

Unsteady aerodynamic effects in small-amplitude pitch oscillations of an airfoil

P. S. Negi, R. Vinuesa, A. Hanifi, P. Schlatter and D. S. Henningson

Department of Mechanics, Linné FLOW Centre and Swedish e-Science Research Centre (SeRC), KTH Royal Institute of Technology, SE-100 44 Stockholm, Sweden

In Proc. 10th Int. Sym. on Turbulence & Shear Flow Phenomenon (TSFP-10 extended version)

High-fidelity wall-resolved large-eddy simulations (LES) are utilized to investigate the flow-physics of small-amplitude pitch oscillations of an airfoil at $Re_c = 100,000$. The investigation of the unsteady phenomenon is done in the context of natural laminar flow airfoils, which can display sensitive dependence of the aerodynamic forces on the angle of attack in certain “off-design” conditions. The dynamic range of the pitch oscillations is chosen to be in this sensitive region. Large variations of the transition point on the suction-side of the airfoil are observed throughout the pitch cycle resulting in a dynamically rich flow response. Changes in the stability characteristics of a leading-edge laminar separation bubble has a dominating influence on the boundary layer dynamics and causes an abrupt change in the transition location over the airfoil. The LES procedure is based on a relaxation-term which models the dissipation of the smallest unresolved scales. The validation of the procedure is provided for channel flows and for a stationary wing at $Re_c = 400,000$.

Key words: unsteady aerodynamics, dynamic-response, transition, wall-resolved les

1. Introduction

A large focus of the research on unsteady wings tends towards stall dynamics such as the earlier works of McCroskey (1981); McCroskey *et al.* (1982); McCroskey (1973); McCroskey *et al.* (1976); Carr *et al.* (1977); Ericsson & Reding (1988a,b), *etc.* More recent works by Dunne & McKeon (2015); Rival & Tropea (2010); Choudhry *et al.* (2014); Visbal (2011, 2014); Visbal & Garmann (2017); Alferez *et al.* (2013); Rosti *et al.* (2016) *etc.* continue the investigation which appears far from complete. The review by McCroskey (1982) and a more recent one by Coorke & Thomas (2015) provide an overview of the dynamic stall process. Studies on the aerodynamic behavior of small-amplitude pitch oscillations are typically done from the perspective of aeroelasticity where investigations tend to focus on the time varying aerodynamic forces on the airfoil with much less

attention paid to the boundary-layer characteristics. Some studies focusing on the time dependent boundary layer in small pitch amplitudes include the work done by Pascazio *et al.* (1996) which shows a time delay in laminar-turbulent transition during pitching. Nati *et al.* (2015) analyzed the effect of small amplitude pitching on a laminar separation bubble at low Reynolds numbers. Mai & Hebler (2011) and Hebler *et al.* (2013) investigate the boundary layer changes in an oscillating natural laminar flow airfoil in transonic conditions. Such cases qualitatively represent small changes in operating conditions, such as

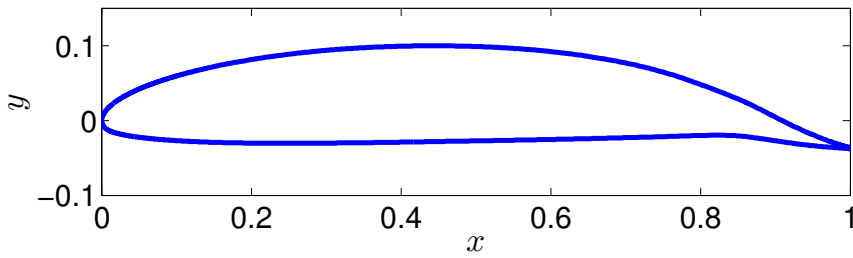


Figure 1: Natural Laminar Flow (NLF) airfoil tested at the Aeronautical and Vehicle engineering department of KTH (Lokatt & Eller 2017; Lokatt 2017)

the changes due to structural deformations or small trailing-edge flap deflections. The understanding of flow response to such changes can be crucial in cases where small perturbations induce large variations in aerodynamic forces. Such sensitive dependence of aerodynamic forces may be found in the static characteristics of natural laminar flow (NLF) airfoils for a certain range of angle of attack. Their performance critically depends on maintaining laminar flow over the suction side of the airfoil and a loss of laminar flow over the airfoil causes large variations of the aerodynamic forces. In addition to such sensitive dependence of the aerodynamic characteristics, recent transonic unsteady experiments using NLF airfoils have brought to light a peculiar property of these airfoils. The unsteady aerodynamic coefficients for laminar airfoils exhibit a non-linear dynamic response to simple harmonic pitch motions (Mai & Hebler 2011; Hebler *et al.* 2013). Such a non-linear response is inconsistent with the predictions of classical unsteady aerodynamic models (Theodorsen 1935). Similar experiments within the subsonic range have been performed by Lokatt (2017) who also found strongly non-linear behavior of the normal force coefficient. These non-linearities occur only for oscillations within a certain range of angle of attack (α) and have been strongly linked to the free movement of transition over the suction side of the airfoil. They seem to be nearly absent when suction side transition is fixed at the leading-edge (Mai & Hebler 2011; Lokatt 2017).

The present work investigates the flow physics of small-amplitude pitch oscillations of a laminar airfoil (figure 1). The airfoil was designed at the Aeronautical and Vehicle Engineering department of KTH, where it has been used in previous experimental and numerical works (Lokatt & Eller 2017). The same airfoil was used in the unsteady experiments of Lokatt (2017). The simulations

are performed at a chord-based Reynolds number of $Re_c = 100,000$. The angle of attack range for the oscillation was chosen from the static characteristics of the airfoil. The static characteristics were calculated using an integral boundary layer code XFOIL (Drela 1989), which predicted sharp changes in the coefficient of moment (C_m) and suction-side transition location (figure 2) above an angle of attack $\alpha > 6^\circ$. The steep slope of the coefficient of moment curve indicates a region where aerodynamic forces are sensitive to small changes in α . The pitch oscillations are performed within this sensitive region. Simulations with a static airfoil are performed to ascertain the exact dynamic range of the pitching motion which is described in section 3.

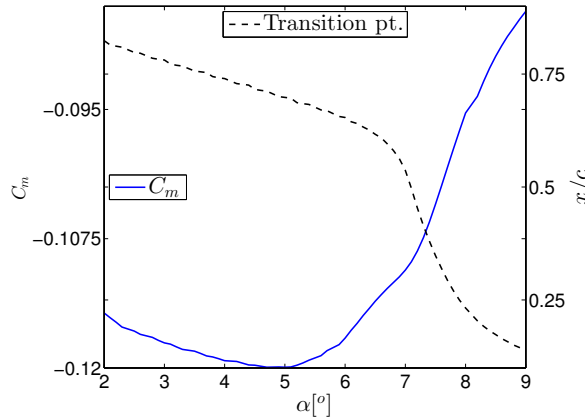


Figure 2: Coefficient of moment (C_m) (values on the left axis), and suction side transition location (values on the right axis) as calculated using XFOIL.

In recent works, wall-resolved large-eddy simulations have proven to be an effective tool for studying flow physics at high Reynolds numbers with a computational cost which is much lower than that of direct numerical simulations (DNS). Some of the works to utilize this method include spatially evolving boundary layers (Eitel-Amor *et al.* 2014), turbulent channel flows (Schlatter *et al.* 2006b,*a*), pipe flows (Chin *et al.* 2015) and flow over wings (Uzun & Hussaini 2010; Lombard *et al.* 2016). Successful application of the approach has motivated its use in the present work, which aims to gain insight into the flow-physics of unsteady airfoils undergoing small amplitude pitch oscillations.

The remainder of the paper is divided into 3 sections. Section 2 describes the numerical setup and presents the results of the validation of the LES. Results of both the stationary and pitching simulations are discussed in Section 3. The conclusions of the study are presented in Section 4.

2. Computational setup

2.1. Numerical method

The computational code used for the simulations is Nek5000, which is an open-source incompressible Navier–Stokes solver developed by Fischer *et al.* (2008) at Argonne National Laboratory. It is based on a spectral-element method which allows the mapping of elements to complex geometries along with a high-order spatial discretization within the elements. The method uses Lagrange interpolants as basis functions and utilizes Gauss–Lobatto–Legendre (GLL) quadrature for the distribution of points within the elements. The spatial discretization is done by means of the Galerkin approximation, following the $P_N\text{--}P_{N-2}$ formulation (Maday & Patera 1989). An 11th order polynomial approximation is used for the velocity with a 9th order approximation for pressure. The nonlinear terms are treated explicitly by third-order extrapolation (EXT3), whereas the viscous terms are treated implicitly by a third-order backward differentiation scheme (BDF3). Aliasing errors are removed with the use of over-integration. The Arbitrary-Lagrangian-Eulerian (ALE) formulation is used to account for the mesh deformation due to the motion of the pitching airfoil (Ho & Patera 1990, 1991). All equations are solved in non-dimensional units with the velocities normalized by the reference free-stream velocity U_0 and the length scales in all directions are normalized by the chord length c . The resultant non-dimensional time unit is given by c/U_0 .

2.2. Relaxation-term large-eddy simulation (RT-LES)

The LES method is based on the RT3D variant of the ADM-RT approach first used by Schlatter *et al.* (2004). The method supplements the governing equations with a dissipative term ($\chi\mathcal{H}(u)$). The equations for the resolved velocity and pressure thus read as

$$\frac{\partial u}{\partial t} + u \cdot \nabla u = -\frac{1}{\rho} \nabla p + \frac{1}{Re} \nabla^2 u - \chi\mathcal{H}(u), \quad (1a)$$

$$\nabla \cdot u = 0, \quad (1b)$$

where \mathcal{H} is a high-pass spectral filter and χ is a model parameter. Together the two parameters determine the strength of the dissipative term. The method has been used in earlier studies of spatially developing boundary layers (Eitel-Amor *et al.* 2014) and channel flows (Schlatter *et al.* 2006b). The method has been shown to be reliable in predicting transition location and also preserving the characteristic structures which are seen in the DNS of transitional flows (Schlatter *et al.* 2006b).

A number of tests were carried out in a channel flow at a friction Reynolds number of $Re_\tau = 395$, and the results are compared with the DNS data of Moser *et al.* (1999). The final mesh was set up such that the streamwise resolution was $\Delta x^+ = 18$ and the spanwise resolution was $\Delta z^+ = 9$. The first point in the wall-normal direction was set at $\Delta y_w^+ = 0.64$ and the wall-normal resolution near the boundary layer edge was $y_{max}^+ = 11$. The superscript $+$ indicates

normalization in inner units. A comparison of the results for the turbulent channel flow is shown for the mean velocity in figure 3a, and for the turbulent kinetic energy (TKE) budget in figure 3b. The dissipation profile shown in the figure is the sum of resolved dissipation and the added dissipation by the relaxation term. A good agreement with the DNS is found for the mean velocity and all the kinetic energy budget terms (including the total dissipation). The resolution used this study is much finer than the typical LES and closer to the coarse DNS resolutions used in the studies of turbulent flows. A very similar resolution is used in the simulation of spatially developing boundary-layer over a flat-plate by Eitel-Amor *et al.* (2014) where the ADM-RT model is used. Similarly, LES cases of pipe flows at $Re_\tau \approx 1000$ by Chin *et al.* (2015) uses slightly coarser resolutions than the one used in the present study.

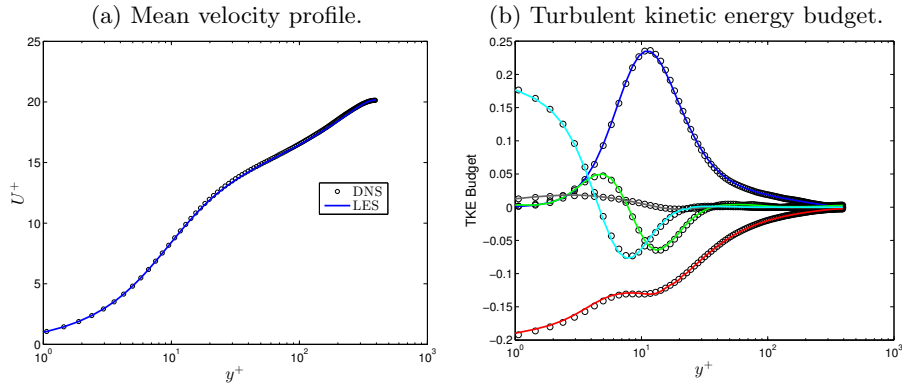


Figure 3: Comparison of mean velocity profile and turbulent kinetic energy budget. Circles represent the DNS data from Moser *et al.* (1999) while the lines represent the values from the LES. All values are normalized with inner units. The individual terms are color coded as: Production (blue), dissipation (red), viscous diffusion (cyan), turbulent diffusion (green), velocity-pressure correlation (gray)

2.3. Mesh generation

The optimum mesh resolution (in inner units) obtained in the channel flow results is then used to design the mesh around the airfoil. Wall-shear stress data is obtained using XFOIL to estimate the grid spacing on the airfoil. A trip is introduced in XFOIL at $x/c \approx 0.1$ to obtain turbulent wall-shear values on both the suction and pressure sides of the airfoil. Here c denotes the chord length. The grid design around the airfoil uses the following criteria:

- For $0.1 < x/c < 0.6$, $\Delta x^+ = 18$, $\Delta y_{wall}^+ = 0.64$ and $\Delta y_{max}^+ = 11$, using the local wall-shear (τ_w) values on the airfoil. Since the flow is expected to be laminar on the pressure side, the stream-wise resolution is slightly relaxed to $\Delta x^+ = 25$ while keeping the same wall-normal resolution.

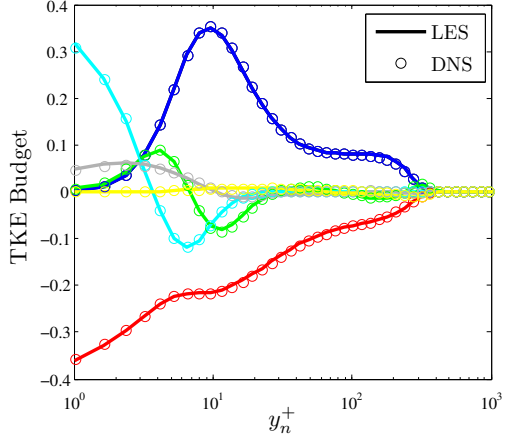


Figure 4: Comparison of turbulent kinetic energy budget for a NACA4412 wing section at the suction side location of $x/c = 0.7$. The circles represent DNS data from Hosseini *et al.* (2016) while the lines are data from the LES. The individual terms are color coded as: Production (blue), dissipation (red), viscous diffusion (cyan), turbulent diffusion (green), velocity-pressure correlation (gray), convection (yellow)

- For $x/c < 0.1$, the peak τ_w value over the suction side of the airfoil is used to estimate the grid spacing.
- For $x/c > 0.6$, the suction side experiences a large adverse pressure gradient which significantly reduces τ_w values. Therefore, the τ_w values from the pressure side are used for both the suction and pressure sides.
- A structured mesh is used, which is extruded in the spanwise direction. Hence the spanwise resolution is constant throughout the domain. The resolution is set to $\Delta z^+ = 9$, where the the peak τ_w value from the suction side is used.

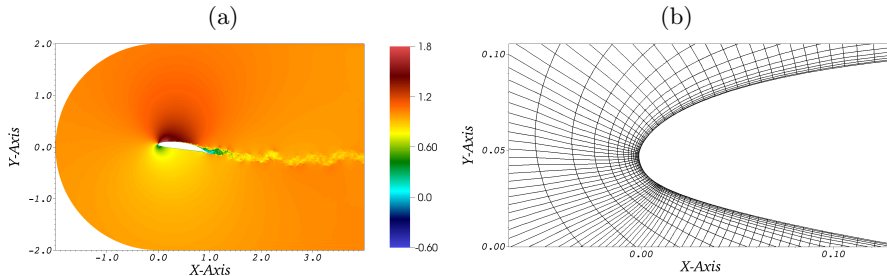


Figure 5: (a) 2D section of the simulation domain. Colors represent the instantaneous streamwise velocity. (b) Close-up view of the spectral-element grid near the airfoil surface.

A different criterion is needed for defining the resolution in the wake where the wall-based criteria are not valid. Accordingly, Reynolds-averaged Navier–Stokes (RANS) simulations were performed using the transition $k\text{--}\Omega$ SST model (Langtry & Menter 2009) with *ANSYS® FLUENT*, to estimate the Kolmogorov length scale (η) in the wake region. The RANS is setup with domain boundaries at a distance of 100 chords from the airfoil. The grid in the wake region for the LES is designed such that the average grid spacing between the GLL points follows the criteria: $\Delta x/\eta < 9$. The computational domain is set up such that the far field boundaries of the computational domain are two chords away from the airfoil leading edge in either direction. The outflow boundary is four chords downstream from the airfoil leading edge and the inlet is designed as a curved inflow boundary with a constant radial distance of two chords from the leading edge of the airfoil. The spanwise width of the domain is $l_z = 0.25$ chords. The domain can be visualized in figure 5a and a close-up view of the spectral-elements is shown in (figure 5b). Each of the spectral-elements are further discretized by $12 \times 12 \times 12$ grid points in 3D, corresponding to an 11th order spectral discretization. Periodic boundary conditions are imposed on the spanwise boundaries, while the energy-stabilized outflow condition suggested by Dong *et al.* (2014) is imposed on the outflow boundary. Velocity field data for locations corresponding to the boundaries of the LES computational domain is extracted from an unsteady RANS simulation. The extracted data is imposed as a Dirichlet boundary condition on these boundaries for the LES. The method is very similar to the one used by Hosseini *et al.* (2016) in their DNS of flow around a wing section. In order to simulate low turbulence flight conditions, free-stream turbulence of intensity $Ti = 0.1\%$ is superimposed on the Dirichlet boundary conditions. The free-stream turbulence is generated using Fourier modes with a von Kármán spectrum. The procedure is similar to the one described in Schlatter (2001); Brandt *et al.* (2004) and Schlatter *et al.* (2008) and has been used for the study of transition in flat plate boundary layers under the influence of free-stream turbulence. The same method has also been used for generating grid-turbulence in simulations of wind-turbines (Kleusberg 2017).

A validation of the above methodology for complex geometries such as a wing section was performed at a chord based Reynolds number of $Re_c = 400,000$ for NACA4412 airfoil. The LES grid resolution was setup with the same grid criteria as described above. The domain boundaries and boundary conditions are identical to the setup in Hosseini *et al.* (2016). A comparison of the wall-normal profiles of the normalized kinetic energy budget is shown in figure 4. The profiles are extracted a streamwise location of $x/c = 0.7$ on the suction side of the airfoil. The LES profiles (lines) match well with the DNS data (circles) of Hosseini *et al.* (2016), signifying the high accuracy of the LES with the current resolution.

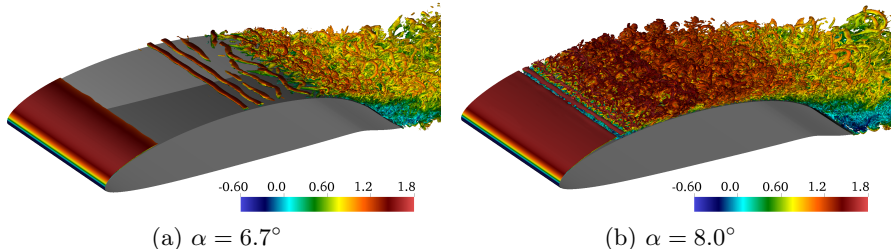


Figure 6: Isocontours of instantaneous λ_2 structures observed for two different (stationary) angles of attack.

3. Results and discussion

3.1. Steady results

Simulations with a stationary airfoil were performed to investigate the location of transition without pitching motion. The simulations were performed for $Re_c = 100,000$ at two different angles of attack ($\alpha = 6.7^\circ$ and $\alpha = 8.0^\circ$). As observed in figure 6, the iso-contours of coherent structures, identified by negative λ_2 method (Jeong & Hussain 1995), show a substantial change in transition location for a small $\Delta\alpha = 1.3^\circ$. For $\alpha = 6.7^\circ$ the strong pressure gradient effects near the trailing edge cause transition at $x/c \approx 0.7$. While for $\alpha = 8.0^\circ$, a leading-edge laminar separation bubble forms, causing flow transition much closer to the leading edge at $x/c \approx 0.2$. Such a leading-edge laminar separation bubble is not observed for the $\alpha = 6.7^\circ$ case. The results are consistent with the trends obtained from XFOIL calculations, showing a large variation in the transition point within a small α change (figure 2).

3.2. Unsteady boundary layer characteristics

Once the static characteristics of the airfoil are obtained, the dynamic effects on the boundary layer are investigated by pitching the airfoil about a mean angle $\alpha_0 = 6.7^\circ$ with an amplitude of $\Delta\alpha = 1.3^\circ$. The reduced frequency of oscillation is $k = 0.5$ and the pitch axis is located at $(x_0, y_0) = (0.35, 0.034)$. The reduced frequency is defined as $k = \Omega b/U_0$, where Ω is the angular frequency of oscillation, b is the semi-chord length and U_0 is the free-stream velocity. The motion of the airfoil is prescribed by equation 2. The pitching motion corresponds to an oscillation time period of $T_{osc} = 2\pi$.

$$\alpha = \alpha_0 + \Delta\alpha \sin(\Omega t). \quad (2)$$

The time variation of the coefficient of lift (C_L) is shown in figure 7. The initial phase of pitching motion is carried out using a lower resolution (polynomial order $N = 5$) to simulate the initial transient period of the flow at a lower computational cost. The polynomial order is then smoothly raised to $N = 11$ before the fourth pitch cycle. Due to the fairly large separation at the trailing edge, effects of transition movement and turbulence, successive pitch cycles are not expected to have identical behavior, however some of qualitatively repeating

trends can be observed. The behavior of the lift coefficient shows a chaotic but qualitatively repeating pattern where C_L shows a smooth increase during the pitch-up motion, with strong secondary effects occurring near the maxima of the pitch cycles. Similarly in the pitch-down phase the lift decreases smoothly with secondary effects again becoming important at the minima of the pitch-cycles.

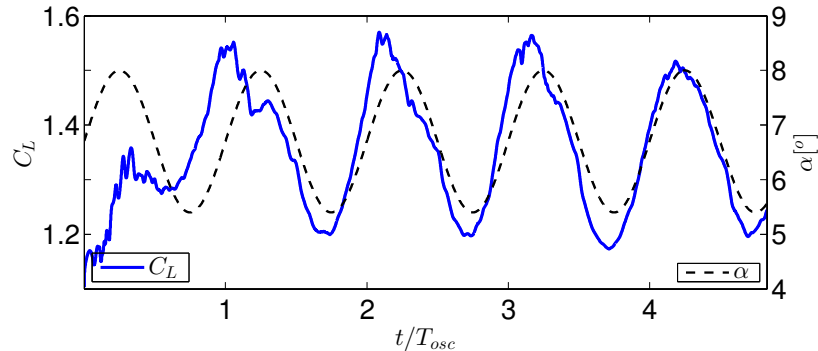


Figure 7: Coefficient of lift (C_L) and angle of attack (α) variation with time. C_L is on the left axis while α is on the right axis.

In order to understand the time variation of the spatially developing boundary layer on the airfoil, we analyze the space-time evolution of the instantaneous spanwise averaged wall-shear stress. The space-time surface plot is shown in figure 8a, which spans the fourth and fifth pitch cycles. The color specifies the value of wall-shear stress on the suction side of the airfoil. Regions with color intensity strongly towards red are indicative of high shear and thus turbulent flow. The exception to the rule being the region close to the leading edge where the flow is laminar but a high shear region exists due to the extremely thin boundary layer close to the stagnation point. The same space-time surface is shown again as a binary colored surface plot in figure 8b, where black colored regions indicate negative wall-shear stress and hence separated flow, while the white region corresponds to locations with attached flow ($\tau_w > 0$).

It is obvious from the two plots in figure 8, that the developing boundary layer on the airfoil exhibits a dynamically rich response to small-amplitude pitch oscillations, with different key boundary layer characteristics controlling the dynamics of the flow in different phases of the pitch cycle. We identify some of the key boundary-layer characteristics to paint an over-all picture of the dynamics. A persistent trailing-edge separation can be identified in figure 8b beyond $x/c > 0.8$. The trailing-edge separation does not exhibit reverse flow 100% of the time, as can be seen from the white patches dispersed between largely black colored regions. An isolated separated region (distinct from the trailing edge separation) is observed at $x/c \approx 0.6$ at times $t/T_{osc} \approx 3$ and $t/T_{osc} \approx 4$. This is identified as a trailing-edge LSB. This LSB is short lived in time, existing for slightly less than a quarter of the pitch-cycle. A large separated region near the leading edge is a leading-edge LSB, similar to the

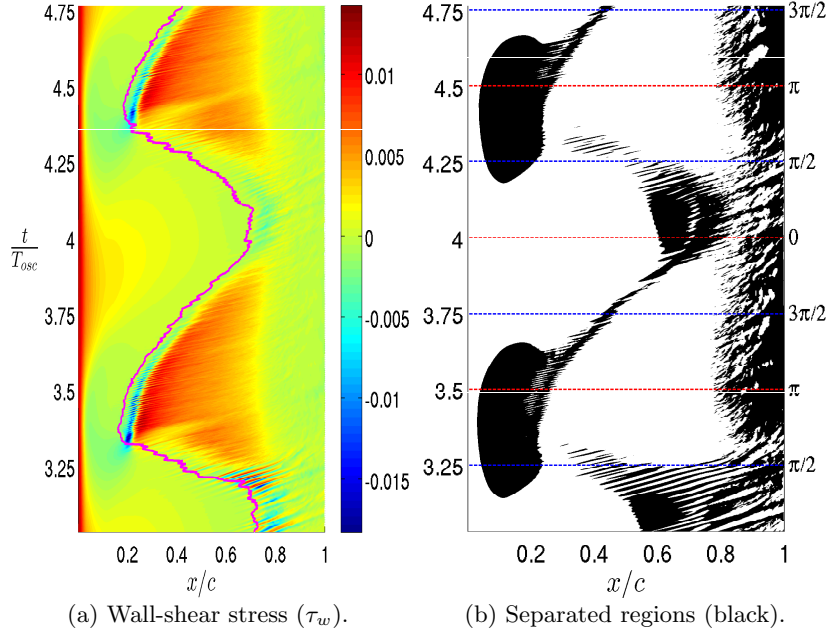


Figure 8: (a) Space-time plot for the wall-shear values (τ_w) and (b) separated flow regions. The values are obtained from the instantaneous flow averaged over the spanwise direction. Magenta line in (a) denotes the calculated transition location. Horizontal blue dashed lines in (b) represent the extrema of the angle of attack, while the red dashed lines represent phases corresponding to mean angle of attack.

one seen in the steady case at $\alpha = 8.0^\circ$. The separation bubble persists much longer in time, spanning nearly half a pitch cycle. Evident from figure 8a is that the transition point changes substantially throughout the pitch cycle. Interestingly, the flow over the airfoil differs significantly during the pitch-up and the pitch-down phases for the same angle of attack. For example, when the instantaneous angle of attack is at phase $\phi = 0$ ($t/T_{osc} = 3, 4$), which represents mean angle of attack but in the pitch-up phase, the flow over the airfoil is mostly laminar up to $x/c \approx 0.7$. On the other hand, for a phase of $\phi = \pi$ ($t/T_{osc} = 3.5, 4.5$), representing the airfoil at the mean angle of attack but in the pitch-down phase, the flow is almost entirely turbulent with the start of the turbulent region approximately at $x/c \approx 0.22$.

3.3. Transition location

In the present work we focus on the variation of transition location throughout the pitch cycles. Since the flow case is unsteady, and the transition location does not remain fixed, a criteria based on the instantaneous state of the flow is needed to determine the transition location. To this end, we calculate statistical

quantities which are averaged in the homogeneous spanwise direction, and also averaged for a short duration (Δt) in time. This averaged value is considered as the “instantaneous” value for that quantity. Thus this instantaneous value of any statistical quantity $\bar{q}(x, y, t)$ can be evaluated as in equation 3:

$$\bar{q}(x, y, t) = \left(\frac{1}{z_{max} - z_{min}} \right) \left(\frac{1}{\Delta t} \right) \int_{t'=t}^{t'=t+\Delta t} \int_{z=z_{min}}^{z=z_{max}} q(x, y, z, t') dz dt'. \quad (3)$$

Here $(z_{max} - z_{min})$ is the spanwise extent of the computational domain. In order for such a quantity to be representative of the instantaneous state of the flow, the time duration of the averaging must be small. For the current case we use $\Delta t = 4 \times 10^{-3}$, which amounts to 0.06% of the oscillation time period during which the flow can be assumed to remain in approximately the same state. Using this procedure we evaluate the fluctuating Reynolds stress, $\overline{u'v'}(x, y, t)$, in order to determine the instantaneous transition location. The first streamwise location (on the suction-side) where the fluctuating Reynolds stress becomes larger than a certain threshold is denoted as the transition point. In order to prescribe a suitable threshold, the maximum value of $|\overline{u'v'}|$ across the entire boundary layer is evaluated for all times. This maximum value does not exhibit large variations, remaining within the same order of magnitude for all times with its mean value being $|\overline{u'v'}|_{max} \approx 0.05$. The threshold for determining transition is set to 5% of this value. The transition point is thus the first point where $|\overline{u'v'}| > 0.0025$. Since we use an ad-hoc criterion for transition location, this is cross-checked by evaluating the variance of the spanwise velocity fluctuations $w'w'$, and following an identical procedure as described above. In this case the transition criterion is prescribed as $|\overline{w'w'}| > 0.005$ since the peak spanwise fluctuation intensities are found to be nearly twice the peak Reynolds stress $|\overline{u'v'}|$. Physically, growing spanwise velocity fluctuations indicate the onset of three-dimensionality in the boundary layer, which are associated with secondary instabilities. The temporal variation and the phase portrait of the calculated transition location using the aforementioned two criteria are shown in figure 9. The magenta line in figure 8 shows the calculated transition locations superposed on the space-time plot of the wall-shear stress. The calculated transition locations are consistent with the picture of wall-shear stress with transition marginally preceding regions of turbulent flow. While the thresholds specified may be considered ad-hoc, the qualitative picture of transition movement is not very sensitive to small changes in the threshold. Changing the thresholds by a factor of 2 still produces the same qualitative trends (not shown). Moreover, the time variation of transition point determined by two different physical quantities agree very well with each other. Thus we consider the quantities as a good representations of instantaneous flow characteristics.

The superposed plots in figure 8 indicate that the two LSBs play a dominating role in the flow dynamics and that transition location is governed by the characteristics of these LSBs. Figure 10 (left) shows the iso-contours of instantaneous vortical structures, identified by the λ_2 method (Jeong & Hussain 1995), at four different times during the pitch-up cycle when the transition is

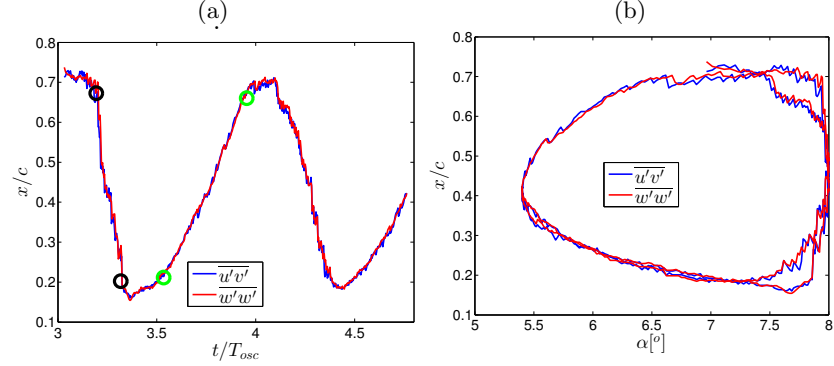


Figure 9: Time variation (a) and phase portrait with α (b) of transition location evaluated using the criteria for $|\overline{u'v'}|$ and $|\overline{w'w'}|$. The circles mark the points used to approximate the upstream (black circles) and downstream (green circles) velocities of the transition point.

moving upstream. This phase is marked by the appearance of a leading-edge LSB which grows in size. The top figure shows the flow state near the mean angle of attack ($t/T_{osc} = 3.09$) during the pitch-up phase. The flow is mostly laminar across the airfoil with no structures observed prior to flow transition and there is no leading-edge LSB. The high adverse pressure gradient near the trailing edge causes the laminar flow to easily separate, forming a LSB and flow transitions over this separated shear layer. Figure 10 (left) from top to bottom shows the part of the oscillation cycle when transition is moving upstream at time instants of $t/T_{osc} = 3.09, 3.2, 3.3$ and 3.47 . Note that pitch-up phase completes at $t/T_{osc} = 3.25$ when the airfoil is at the highest angle of attack. Thus upstream movement of transition starts nearly at the end of the pitch-up phase and continues to move upstream even during the pitch-down cycle. The laminar separation bubble close to the trailing edge ceases to exist as transition moves upstream. At $t/T_{osc} = 3.47$ the flow transition is seen to occur on the separated shear layer of the leading-edge LSB (bottom left in figure 10).

As the airfoil progresses through the pitch-down cycle the leading-edge LSB shrinks in size and the transition point then starts moving downstream, initiating the process of flow re-laminarization (figure 10 right, top to bottom). The leading-edge LSB eventually disappears, although the transition point moves downstream of the LSB before it completely disappears. The flow over the airfoil is not completely re-laminarized even when the airfoil is at the lowest angle of attack and the re-laminarization process continues into the pitch-up phase. There is a marked asymmetry between the upstream and downstream movement of the transition point. An approximate velocity for both the upstream and downstream motion of the transition point is calculated across the points marked by circles in figure 9a which correspond to transition movement with near constant velocity. The velocity of upstream transition

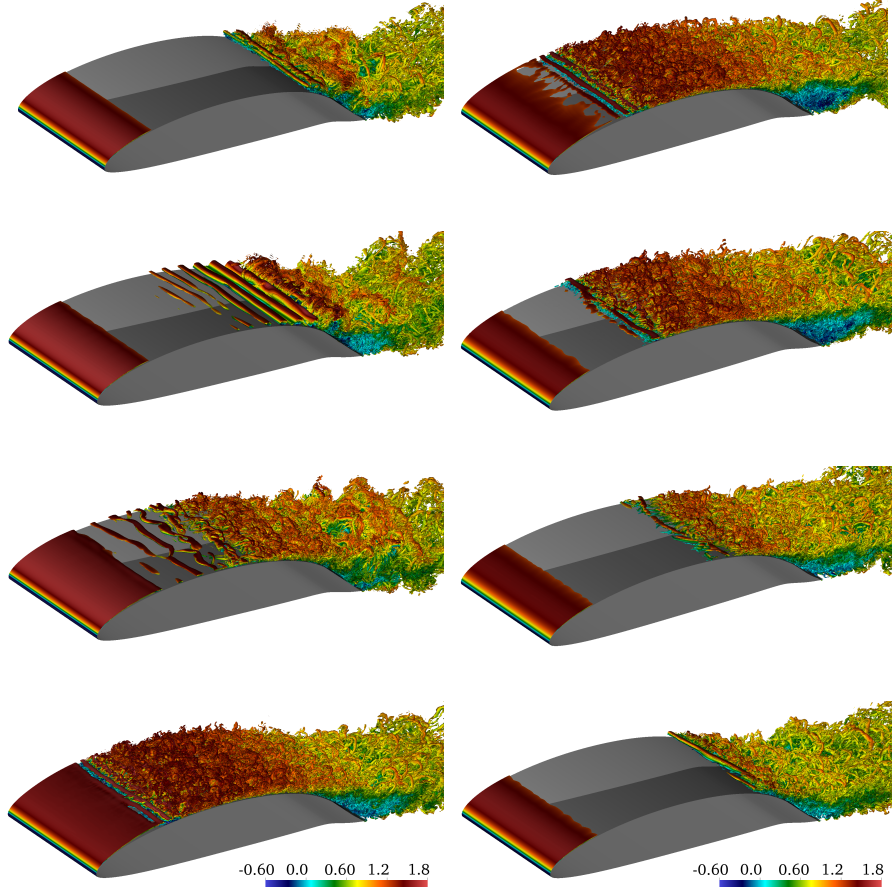


Figure 10: Visualization of instantaneous λ_2 structures at different phases of the pitch cycle. The figures on the left are during the phase of the pitch cycle when the transition is moving upstream. From top to bottom the time-stamps of the instantaneous snapshots correspond to a normalized flow time of $t/T_{osc} = 3.09, 3.2, 3.3, 3.47$. On the right the instantaneous snapshot correspond to the re-laminarization phase as transition moves downstream. The time-stamps from top to bottom on the right correspond to $t/T_{osc} = 3.55, 3.63, 3.82, 4.01$

movement is calculated across the black circles and is equal to $V_u^{tr} = -0.60$ while the velocity of the downstream motion of transition is calculated across the green circles and is equal to $V_d^{tr} = 0.17$. Thus the upstream spread of turbulent regions is much faster than flow re-laminarization.

Specifying a velocity of transition movement implies that the transition location changes smoothly with time. This is true for the downstream movement

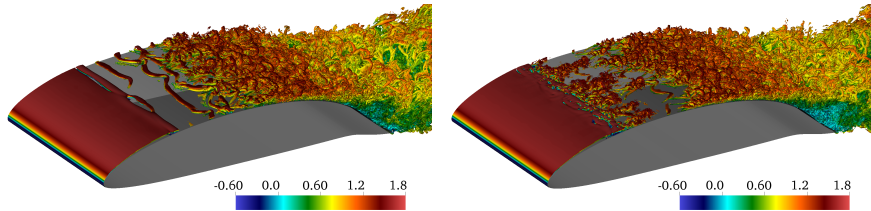


Figure 11: Comparison of boundary layer transition at two different time instants of $t/T_{osc} = 3.33$ (left) and $t/T_{osc} = 3.35$ (right).

of transition, however the final stages of the upstream movement appear to be more complex. Figure 11 shows the instantaneous vortical structures at two time instants during the upstream movement phase. In the left figure ($t/T_{osc} = 3.33$) a single connected region of turbulence can be observed which is preceded by a laminar region identified by the near absence of small vortical structures. This region starts at about 40% and the entire boundary layer downstream is turbulent. On the right figure ($t/T_{osc} = 3.35$) there is a similar large connected region of turbulence, spreading from approximately 40% of the chord. However there is also a nascent region of turbulence starting at $x/c \approx 0.2$. These two regions are separated by a patch of laminar flow. The figure on the right then has two distinct locations where transition to turbulence takes place. After a short while, turbulence spreads downstream from this newly formed transition location and eventually the entire boundary layer downstream is turbulent. This flow state, where two distinct turbulent regions can be identified exists only for a short duration and by $t/T_{osc} = 3.4$ no intermediate regions of laminar flow can be identified. However the emergence of two distinct transition locations indicates that at least two competing mechanisms exist for the growth of disturbances in the boundary layer and that their relative strength changes during the pitch cycle. Given that this new transition occurs at the separated shear layer of the leading-edge LSB, the stability properties of the LSB are likely to play a role in the emergence of this new transition point.

3.4. Stability characteristics of the laminar separation bubble

The stability characteristics of the leading-edge LSB can help shed some light on the changing transition locations throughout the pitch cycle and in particular on the existence of competing mechanisms for transition. The competition between convective and absolute instability characteristics may provide a possible explanation for the transient existence of two distinct points of transition. The change of flow state from laminar to turbulent is often governed by the linear amplification of small disturbances within the boundary layer. For flows with streamwise and spanwise homogeneity the evolution of small perturbations

within the boundary layer is governed by the Orr-Sommerfeld equation

$$\left[\left(\frac{\partial}{\partial t} + U \frac{\partial}{\partial x} \right) \nabla^2 - U'' \frac{\partial}{\partial x} - \frac{1}{Re} \nabla^4 \right] v = 0, \quad (4)$$

where v is wall-normal component of the velocity fluctuations and U'' is the second derivative in the wall-normal direction of the streamwise velocity U . Due to Squire's theorem, analyzing the two-dimensional perturbations is sufficient to study the modal stability characteristics. Following Schmid & Henningson (2001) and assuming an ansatz function for the wall-normal perturbations as

$$v = \tilde{v}(y) e^{i(k_x x - \lambda t)}, \quad (5)$$

results in a dispersion relation between the complex frequency λ and the streamwise wavenumber k_x given by

$$\left[(-i\lambda + ik_x U)(\mathcal{D}^2 - k_x^2) - ik_x U'' - \frac{1}{Re} (\mathcal{D}^2 - k_x^2)^2 \right] \tilde{v} = 0. \quad (6)$$

Here \mathcal{D} represents the derivative in the wall-normal (y) direction. While strictly valid for homogeneous flows, the Orr-Sommerfeld equation has often been used for flows that exhibit weak inhomogeneity such as the Blasius boundary layer and also for the case of laminar separation bubbles (Alam & Sandham 2000; Hammond & Redekopp 1998; Häggmark *et al.* 2001). A temporal stability analysis using a real spatial wavenumber k_x results in an eigenvalue problem for the frequency λ . Resulting complex frequencies with a positive imaginary part signify that the boundary layer is unstable and that small perturbations within the boundary layer would grow in time and cause transition.

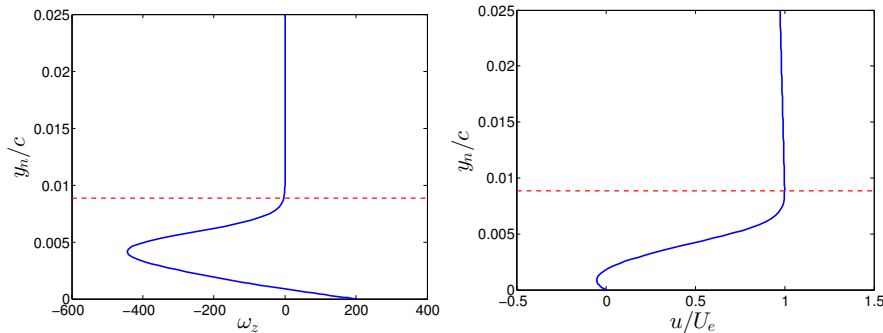


Figure 12: Wall-normal profiles of vorticity (left) and tangential velocity (right) observed in the leading-edge LSB at $t/T_{osc} = 3.25$. Dashed lines mark the boundary layer edge. y_n is the distance along the local wall-normal direction.

To explore the time varying stability properties of the LSB, temporal stability analysis of the Orr-Sommerfeld equations is performed using the instantaneous wall-normal profiles of tangential velocity, calculated as per equation 3. Several velocity profiles can be considered for local analysis. Alam & Sandham (2000) and Häggmark *et al.* (2001) in their local analysis associate

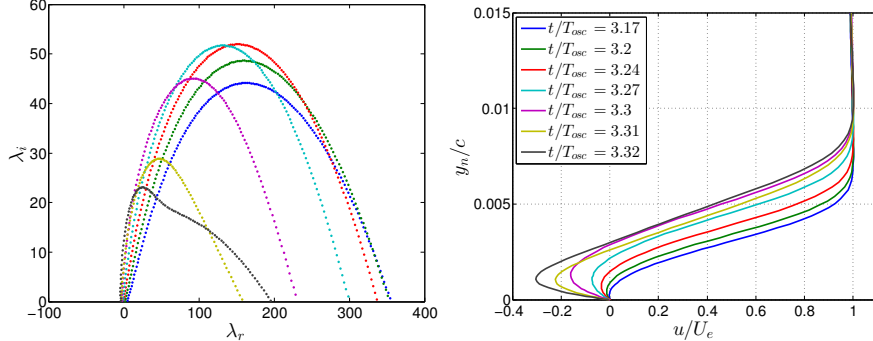


Figure 13: Unstable eigenvalues (left) obtained from a temporal stability analysis for different instantaneous velocity profiles (right).

the stability characteristics of the LSB with the maximum reverse flow intensities. In accordance with the previous studies, we focus on the wall-normal profiles of tangential velocity which exhibit the maximum reverse flow intensity relative to the boundary layer edge velocity. The edge velocity of the local profiles was determined using the criterion of vanishing spanwise vorticity *i.e.* $\bar{\omega}_z \approx 0$. Since there is a very small but finite amount of vorticity in the far-field due to the free-stream turbulence, the criterion for boundary layer height is set as the wall-normal distance where the vorticity decays to 1% of its maximum value in the boundary layer. Figure 12 shows the wall-normal profiles of tangential velocity and spanwise vorticity along with the evaluated height of the boundary layer.

Figure 13 shows the unstable complex frequencies obtained from the temporal stability analysis (with varying k_x) for instantaneous profiles at several different time instants in the fourth pitch cycle. The reverse-flow intensity continues to increase with time until flow transition occurs at the LSB. The flow is unstable for all the analyzed velocity profiles as shown by the existence of complex frequencies with a positive imaginary part. However the highest amplification rate (frequency with maximum imaginary part) does not monotonically increase with reverse-flow intensity. At first the maximum amplification rate increases in time, but later it is seen to decrease. This changing characteristics can be associated with structural changes in the LSB, where at first the region of maximum reverse-flow is found near the center of the LSB, but as the LSB grows in size, this region of strong reverse flow moves closer to the downstream end of the LSB. Such qualitative changes in the shape of the LSB can be seen in figure 14. Structural changes in the LSB and its stability characteristics have previously been linked in the works of Theofilis *et al.* (2000); Cherubini *et al.* (2010) and Rodríguez & Theofilis (2010).

While the local stability analysis show that the boundary layer is unstable, an additional distinction needs to be made with regards to the nature of the instability which may be classified as either convective or absolute (Briggs 1964). The instability characteristics are usually elucidated using the simple concept of

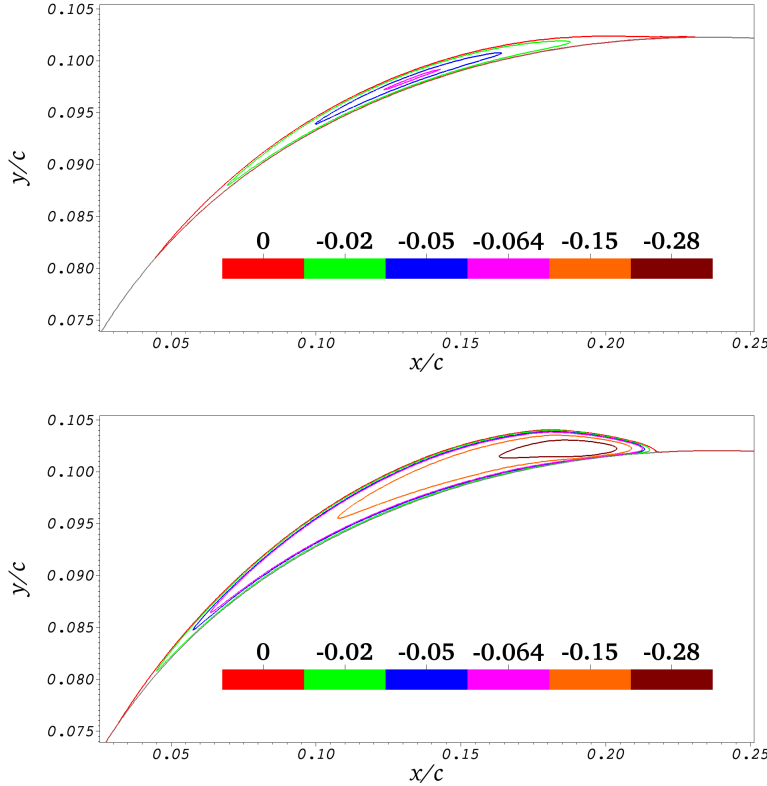


Figure 14: Contours of negative streamwise velocity in the leading-edge LSB at $t/T_{osc} = 3.25$ (top) and $t/T_{osc} = 3.32$ (bottom).

group velocity of perturbations, C_g . Growing perturbations that travel with a positive group velocity are deemed convectively unstable since they move away from the source of disturbance. On the other hand perturbations with zero group velocity are referred to as absolutely unstable, since they do not convect away from the origin of instability and create a self-sustaining process of perturbation growth. In the context of LSBs, high reverse-flow intensity has been associated with the presence of an absolute instability. Alam & Sandham (2000) with their local stability analysis of a two-parameter family of reverse flow profiles indicated that reverse flow intensities above 15% may cause the flow to be locally absolutely unstable. With a similar analysis on a three parameter family of profiles Hammond & Redekopp (1998) obtained onset of absolute instabilities at 20% reverse flow velocities. In the same study the authors also performed global stability analysis on a synthetically created boundary layer with a symmetric separation bubble and found the flow to be globally unstable for 30% reverse flow velocities. Figure 15 shows the absolute value of the maximum reverse flow intensity in the leading-edge LSB found in the present study. The reverse flow

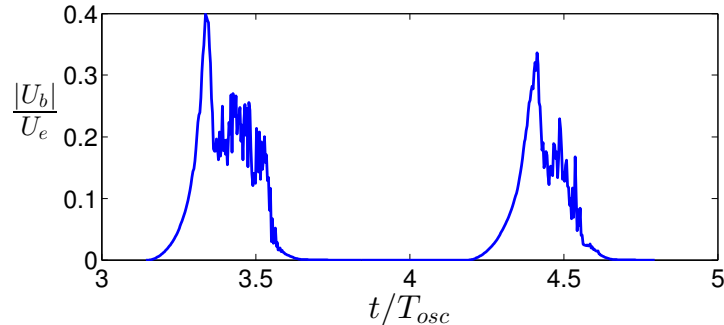


Figure 15: Ratio of maximum reverse flow (U_b) in the leading-edge LSB to the boundary layer edge velocity (U_e).

velocities are found to be higher than 30% in both the fourth and fifth pitch cycles, which is higher than the thresholds indicated by earlier investigators for absolute instability. In such a case it is likely that the leading-edge LSB changes character to become absolutely unstable during the pitch cycle. The change of characteristics may explain the simultaneous existence of two different transition points in the boundary layer. Initially when the reverse-flow intensity in the LSB is small, the flow is convectively unstable and perturbations grow while traveling downstream. Thus transition occurs downstream of the LSB. As the reverse-flow intensity becomes larger, the region of absolute instability may exist within the LSB which would cause perturbations to grow in time without being convected away. When these perturbations grow large they would cause transition over the LSB. Thus momentarily, there would be two distinct transition points, one due to the growth of absolute instabilities in the LSB and one due to convectively amplifying disturbances which cause transition downstream of the LSB.

To explore such a possibility, from the local stability analysis, one needs to identify unstable modes with zero group velocity. Briggs (1964) proposed a general method for the identification of absolute instabilities in a system which is commonly referred to as the Briggs method. The method involves solving the spatial stability problem for a range of complex λ , thus mapping contours on the complex frequency plane onto the complex wavenumber plane through the dispersion relation. Saddle points obtained in the complex wavenumber plane are the points where the dispersion relation has a double root. These points are known as the “pinch-points” in the complex wavenumber plane where the branches corresponding to the forward and backward propagating solutions of the dispersion relation meet via a double root. These pinch points correspond to perturbation modes that have zero group velocity. The mapping of the saddle-point on the frequency plane gives the absolute frequency λ^0 . If this absolute frequency lies in the unstable half of the plane, then the system exhibits an absolute instability. Kupfer *et al.* (1987) proposed the inverse method called the cusp-map method, which maps contours in the complex wavenumber plane

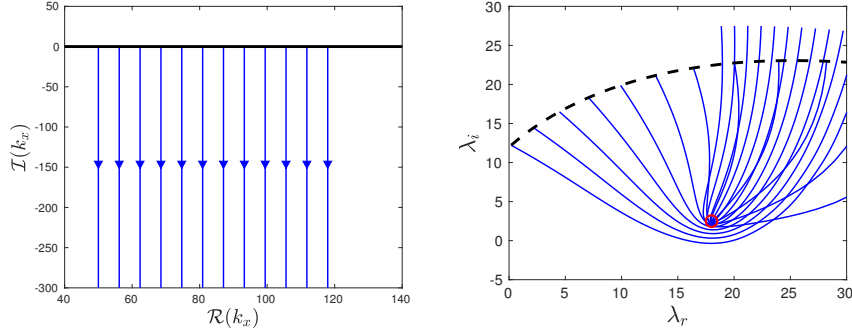


Figure 16: Contours on the complex wavenumber plane (left) and their corresponding mapping onto the complex frequency plane (right) at $t/T_{osc} = 3.32$. Figure on the right shows the unstable cusp associated with absolute instability, located at $\lambda^0 = 18.02 + 2.46i$ (red circle). The dashed black line in the right figure corresponds to solutions of the Orr-Sommerfeld equation for real k_x (black line on the left).

on to the complex frequency plane via the dispersion relation and identified the absolute instability by locating the cusp in the complex frequency plane. This allowed for solving the simpler linear eigenvalue problem for λ rather than the non-linear eigenvalue problem for k_x in the Briggs method (Briggs 1964). Several contours need to be mapped from the wavenumber to the frequency plane for the location of the cusp. Kupfer *et al.* (1987) proposed mapping contours along lines with constant real part of k_x . Figure 16 and 17 show the cusps obtained in the complex frequency plane for the profiles with the highest reverse-flow intensity of tangential velocity. In the fourth cycle at $t/T_{osc} = 3.32$ an unstable cusp is obtained with a positive absolute amplification rate of $\lambda_i^0 = 2.46$. On the other hand the cusp found in the fifth cycle is just marginally stable with an absolute amplification rate of $\lambda_i^0 = -0.5$ at $t/T_{osc} = 4.4$. Since the velocity profiles considered here are averaged values instead of stationary base-flow profiles, it is possible that small temporal variation and/or non-linear modification of the flow hides the absolute instability properties when an averaged flow-field is considered. Nonetheless the results provide a strong indication that the LSB changes character to become absolutely unstable during the pitch cycle.

Caution needs to be taken in the interpretation of the stability analysis. The local stability analysis using the Orr-Sommerfeld equations assumes stationary homogeneous base state. Neither of which are strictly fulfilled when using the instantaneous, spanwise averaged velocity profiles. One can compare the properties of the LSB and the instability time-scales to judge the validity of the such an analysis. The ratio of the time-period of the absolute instability (4^{th} cycle) to the time period of oscillation is 0.05, suggesting that the boundary layer would appear nearly stationary to the amplifying disturbances. For the spatial inhomogeneity, the ratio of the maximum boundary layer height to the length of the separation bubble can be used as an indicator. This ratio is

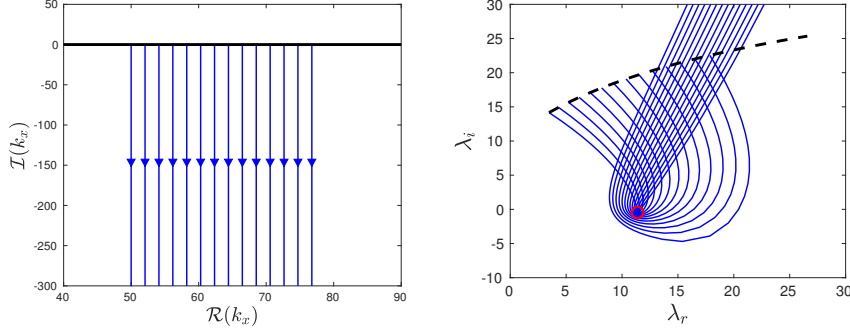


Figure 17: Contours on the complex wavenumber plane (left) and their corresponding mapping onto the complex frequency plane (right) at $t/T_{osc} = 4.40$. Figure on the right shows the marginally stable cusp located at located at $\lambda^0 = 11.41 - 0.49i$ (red circle).

equal to $\delta^{max}/L_x = 0.03$ which suggests a weak spatial inhomogeneity. Here δ^{max} is the maximum value of the boundary layer height over the LSB and L_x is the spatial extent of the LSB. Both the above quantities indicate the quasi-steady, homogeneous flow assumptions may be used to obtain qualitative features of the flow case. The analysis then suggests that the convective instability properties of the boundary layer initially become stronger as the LSB grows in size. Structural changes occur in the LSB as it grows in size with regions of high reverse-flow moving to the end of the bubble. At high reverse-flow intensities the LSB changes character and exhibits a region of absolute instability. This can potentially explain the emergence of two distinct transition locations. The upstream transition would be caused by the temporally growing instabilities which amplify within the region of absolute instability without being convected downstream. On the other hand spatially growing waves associated with convective instabilities would trigger transition further downstream of the LSB. The emergence of the second transition point associated with absolute instabilities would cause abrupt changes in the boundary layer characteristics.

4. Conclusion

A relaxation-term filtering procedure is used for wall-resolved LES of flow over a pitching airfoil. Validation of the LES procedure is done in a channel flow at $Re_\tau = 395$ and for a wing section at $Re_c = 400,000$ and the results show a good agreement with available DNS data sets.

Flow over an airfoil is simulated using the LES procedure at a chord based Reynolds number of $Re_c = 100,000$ within an angle of attack range where the aerodynamic forces on the airfoil exhibit sensitive dependence on the angle of attack. This sensitive dependence is captured in the steady simulations at different angles of attack with large changes in transition location within a small variation of α .

Pitch oscillations of the airfoil within this α range of sensitive dependence displays a rich variety of unsteady flow phenomena. The flow goes through alternating periods of fully turbulent and laminar flow over the suction-side of the airfoil with different governing mechanisms for transition through the oscillating phases. When the flow is mostly laminar over the airfoil surface it separates easily under the effect of adverse pressure gradient, forming an LSB near the trailing-edge. Flow transition occurs over this separated shear layer. As the angle of attack increases, a leading-edge LSB is formed which first excites spatially growing waves (convective instability) causing transition downstream of the LSB. Initially the amplification rate of these spatially growing waves increases as the size of the LSB grows causing transition to move upstream. Eventually a region of absolute instability develops within the LSB and flow transition occurs abruptly on the separated shear layer. When transition is first triggered by this absolute instability mechanism the flow exhibits two distinct transition locations and abrupt changes in the boundary layer follow.

In the pitch-down cycle, the reverse phenomenon occurs where the leading-edge LSB shrinks in size and the region of absolute instability ceases to exit. The transition is then again governed by spatially amplifying waves. The spatial amplification rate now reduces as the LSB shrinks and transition moves downstream. The flow thus goes through states of convective and absolute instability, leading to constantly changing transition location. The upstream and downstream velocities of the transition point movement however are vastly different, with an average upstream velocity being around $V_u^{tr} \approx -0.60$ and a much slower downstream velocity of $V_d^{tr} \approx 0.17$. This asymmetry is yet to be investigated, but may be an important parameter in unsteady turbulence modeling.

Acknowledgement

The computations were performed on resources provided by the Swedish National Infrastructure for Computing (SNIC) at the PDC Center for High Performance Computing at the Royal Institute of Technology (KTH). Simulation have also been performed at the Barcelona Supercomputing Center, Barcelona, with computer time provided by the 12th PRACE Project Access Call (number 2015133182). The work was partially funded by European Research Council under grant agreement 694452-TRANSEP-ERC-2015-AdG. The work was also partially funded by Vinnova through the NFFP project UMTAPS, with grant number 2014-00933. We would like to thank Dr. David Eller and Dr. Mikaela Lokatt for providing us with the NLF design and the numerous discussions on different aerodynamic aspects of the project.

REFERENCES

- ALAM, M. & SANDHAM, N. D. 2000 Direct numerical simulation of 'short' laminar separation bubbles with turbulent reattachment. *Journal of Fluid Mechanics* **410**, 1–28.

- ALFEREZ, N., MARY, I. & LAMBALLAIS, E. 2013 Study of stall development around an airfoil by means of high fidelity large eddy simulation. *Flow, Turbulence and Combustion* **91** (3), 623–641.
- BRANDT, L., SCHLATTER, P. & HENNINGSON, D. S. 2004 Transition in boundary layers subject to free-stream turbulence. *Journal of Fluid Mechanics* **517**.
- BRIGGS, R. J. 1964 *Electron-Stream Interaction with Plasmas*. The MIT Press, Cambridge, Massachusetts.
- CARR, L. W., MCALISTER, K. W. & MCCROSKEY, W. J. 1977 Analysis of the development of dynamic stall based on oscillating airfoil experiments. *Tech. Rep.* NASA Ames Research Center; Moffett Field, CA, United States.
- CHERUBINI, S., ROBINET, J.-C. & PALMA, P. D. 2010 The effects of non-normality and nonlinearity of the navier–stokes operator on the dynamics of a large laminar separation bubble. *Physics of Fluids* **22** (1), 014102.
- CHIN, C., NG, H., BLACKBURN, H., MONTY, J. & OOI, A. 2015 Turbulent pipe flow at $Re_\tau = 1000$: A comparison of wall-resolved large-eddy simulation, direct numerical simulation and hot-wire experiment. *Computers and Fluids* **122**, 26 – 33.
- CHOUDHRY, A., LEKNYS, R., ARJOMANDI, M. & KELSO, R. 2014 An insight into the dynamic stall lift characteristics. *Experimental Thermal and Fluid Science* **58**, 188 – 208.
- COORKE, T. C. & THOMAS, F. O. 2015 Dynamic stall in pitching airfoils: Aerodynamic damping and compressibility effects. *Annual Review of Fluid Mechanics* **47** (1), 479–505.
- DONG, S., KARNIADAKIS, G. E. & CHRYSOSTOMIDIS, C. 2014 A robust and accurate outflow boundary condition for incompressible flow simulations on severely-truncated unbounded domains. *Journal of Computational Physics* **261**, 83–105.
- DRELA, M. 1989 *XFOIL: An Analysis and Design System for Low Reynolds Number Airfoils*, pp. 1–12. Berlin, Heidelberg: Springer Berlin Heidelberg.
- DUNNE, R. & McKEON, B. J. 2015 Dynamic stall on a pitching and surging airfoil. *Experiments in Fluids* **56** (8), 157.
- EITEL-AMOR, G., ÖRLÜ R. & SCHLATTER, P. 2014 Simulation and validation of a spatially evolving turbulent boundary layer up to $Re_\theta = 8300$. *International Journal of Heat and Fluid Flow* **47**, 57–69.
- ERICSSON, L. & REDING, J. 1988a Fluid mechanics of dynamic stall part i. unsteady flow concepts. *Journal of Fluids and Structures* **2** (1), 1 – 33.
- ERICSSON, L. & REDING, J. 1988b Fluid mechanics of dynamic stall part ii. prediction of full scale characteristics. *Journal of Fluids and Structures* **2** (2), 113 – 143.
- FISCHER, P. F., LOTTES, J. W. & KERKEMEIER, S. G. 2008 Nek5000 web page. <http://nek5000.mcs.anl.gov>.
- HÄGGMARK, C. P., HILDINGS, C. & HENNINGSON, D. S. 2001 A numerical and experimental study of a transitional separation bubble. *Aerospace Science and Technology* **5** (5), 317–328.
- HAMMOND, D. & REDEKOPP, L. 1998 Local and global instability properties of separation bubbles. *European Journal of Mechanics - B/Fluids* **17** (2), 145 – 164.
- HEBLER, A., SCHOJDA, L. & MAI, H. 2013 Experimental investigation of the aeroelastic behavior of a laminar airfoil in transonic flow. In *Proceedings IFASD*.
- HO, L.-W. & PATERA, A. T. 1990 A Legendre spectral element method for simulation

- of unsteady incompressible viscous free-surface flows. *Computer Methods in Applied Mechanics and Engineering* **80** (1), 355 – 366.
- HO, L.-W. & PATERA, A. T. 1991 Variational formulation of three-dimensional viscous free-surface flows: Natural imposition of surface tension boundary conditions. *International Journal for Numerical Methods in Fluids* **13** (6), 691–698.
- HOSSEINI, S. M., VINUESA, R., SCHLATTER, P., HANIFI, A. & HENNINSON, D. S. 2016 Direct numerical simulation of the flow around a wing section at moderate Reynolds number. *International Journal of Heat and Fluid Flow* **61**, 117 – 128.
- JEONG, J. & HUSSAIN, F. 1995 On the identification of a vortex. *Journal of Fluid Mechanics* **285**.
- KLEUSBERG, E. 2017 Wind turbine simulations using spectral elements. Licentiate thesis, Royal Institute of Technology (KTH), Stockholm, Sweden.
- KUPFER, K., BERS, A. & RAM, A. K. 1987 The cusp map in the complex-frequency plane for absolute instabilities. *The Physics of Fluids* **30** (10), 3075–3082.
- LANGTRY, R. B. & MENTER, F. R. 2009 Correlation-Based Transition Modeling for Unstructured Parallelized Computational Fluid Dynamics Codes. *AIAA Journal* **47**, 2894–2906.
- LOKATT, M. 2017 On aerodynamic and aeroelastic modeling for aircraft design. Doctoral thesis, KTH Royal Institute of Technology.
- LOKATT, M. & ELLER, D. 2017 Robust viscous-inviscid interaction scheme for application on unstructured meshes. *Computers & Fluids* **145**, 37 – 51.
- LOMBARD, J.-E. W., MOXEY, D., SHERWIN, S. J., HOESSLER, J. F. A., DHANDAPANI, S. & TAYLOR, M. J. 2016 Implicit Large-Eddy Simulation of a Wingtip Vortex. *AIAA Journal* **54**, 506–518.
- MADAY, Y. & PATERA, A. T. 1989 Spectral element methods for the incompressible Navier-Stokes equations. In *State-of-the-art surveys on computational mechanics (A90-47176 21-64)*. New York, American Society of Mechanical Engineers, 1989, p. 71-143. Research supported by DARPA., pp. 71–143.
- MAI, H. & HEBLER, A. 2011 Aeroelasticity of a laminar wing. In *Proceedings IFASD*. Paris.
- MCCROSKEY, W. J. 1973 Inviscid flowfield of an unsteady airfoil. *AIAA Journal* **11** (8), 1130 – 1137.
- MCCROSKEY, W. J. 1981 Phenomenon of dynamic stall. *Tech. Rep.* NASA Ames Research Center; Moffett Field, CA, United States.
- MCCROSKEY, W. J. 1982 Unsteady airfoils. *Annual Review of Fluid Mechanics* **14** (1), 285–311.
- MCCROSKEY, W. J., CARR, L. W. & MCALISTER, K. W. 1976 Dynamic stall experiments on oscillating airfoils. *AIAA Journal* **14** (1), 57 – 63.
- MCCROSKEY, W. J., MCALISTER, K. W., CARR, L. W. & PUCCI, S. L. 1982 An experimental study of dynamic stall on advanced airfoil sections. volume 1: Summary of the experiment. *Tech. Rep.* NASA Ames Research Center, Moffett Field, CA, United States.
- MOSER, R. D., KIM, J. & MANSOUR, N. N. 1999 Direct numerical simulation of turbulent channel flow up to $Re_\tau = 590$. *Physics of Fluids* **11** (4), 943–945.
- NATI, A., DE KAT, R., SCARANO, F. & VAN OUDHEUSDEN, B. W. 2015 Dynamic pitching effect on a laminar separation bubble. *Experiments in Fluids* **56** (9), 172.

- PASCAZIO, M., AUTRIC, J., FAVIER, D. & MARESCA, C. 1996 Unsteady boundary-layer measurement on oscillating airfoils-transition and separation phenomena in pitching motion. In *34th Aerospace Sciences Meeting and Exhibit*, p. 35.
- RIVAL, D. & TROPEA, C. 2010 Characteristics of pitching and plunging airfoils under dynamic-stall conditions. *Journal of Aircraft* **47** (1), 80–86.
- RODRÍGUEZ, D. & THEOFILIS, V. 2010 Structural changes of laminar separation bubbles induced by global linear instability. *Journal of Fluid Mechanics* **655**, 280–305.
- ROSTI, M. E., OMIDYEGANEH, M. & PINELLI, A. 2016 Direct numerical simulation of the flow around an aerofoil in ramp-up motion. *Physics of Fluids* **28** (2), 025106.
- SCHLATTER, P. 2001 Direct numerical simulation of laminar-turbulent transition in boundary layer subject to free-stream turbulence. Diploma thesis, Royal Institute of Technology (KTH), Stockholm, Sweden.
- SCHLATTER, P., BRANDT, L., DE LANGE, H. C. & HENNINSON, D. S. 2008 On streak breakdown in bypass transition. *Physics of Fluids* **20** (10), 101505.
- SCHLATTER, P., STOLZ, S. & KLEISER, L. 2004 LES of transitional flows using the approximate deconvolution model. *International Journal of Heat and Fluid Flow* **25** (3), 549 – 558, turbulence and Shear Flow Phenomena (TSFP-3).
- SCHLATTER, P., STOLZ, S. & KLEISER, L. 2006a *Analysis of the SGS energy budget for deconvolution- and relaxation-based models in channel flow*, pp. 135–142. Dordrecht: Springer Netherlands.
- SCHLATTER, P., STOLZ, S. & KLEISER, L. 2006b Large-eddy simulation of spatial transition in plane channel flow. *Journal of Turbulence* **7**, N33.
- SCHMID, P. J. & HENNINSON, D. S. 2001 *Stability and Transition in Shear Flows*. Springer.
- THEODORSEN, T. 1935 General theory of aerodynamic instability and the mechanism of flutter. *Tech. Rep.*. National Advisory Committee for Aeronautics; Langley Aeronautical Lab.; Langley Field, VA, United States.
- THEOFILIS, V., HEIN, S. & DALLMANN, U. 2000 On the origins of unsteadiness and three-dimensionality in a laminar separation bubble. *Philosophical Transactions of the Royal Society of London A: Mathematical, Physical and Engineering Sciences* **358** (1777), 3229–3246.
- UZUN, A. & HUSSAINI, M. Y. 2010 Simulations of vortex formation around a blunt wing tip. *AIAA Journal* **48**, 1221–1234.
- VISBAL, M. R. 2011 Numerical investigation of deep dynamic stall of a plunging airfoil. *AIAA Journal* **49** (10), 2152 – 2170.
- VISBAL, M. R. 2014 Analysis of the onset of dynamic stall using high-fidelity large-eddy simulations. In *52nd Aerospace Sciences Meeting, AIAA SciTech Forum*. AIAA.
- VISBAL, M. R. & GARMANN, D. J. 2017 Numerical investigation of spanwise end effects on dynamic stall of a pitching naca 0012 wing. In *55th AIAA Aerospace Sciences Meeting, AIAA SciTech Forum*. AIAA.